AGU
ADVANCING
EARTH AND
SPACE SCIENCES

Key Points:

- Production of a 10-unit Spectral Units map conveying the spectral and compositional properties within the Tsiolkovskiy crater
- Integration of geologic and spectral units to produce a more comprehensive mapping product, namely a geo-stratigraphic map
- Elaboration on the geological and compositional evolution of our study area

Author Contributions:

Conceptualization: Gloria Tognon, Francesca Zambon, Matteo Massironi
Data curation: Gloria Tognon, Francesca Zambon, Jean-Philippe Combe, Sergio Fonte
Formal analysis: Gloria Tognon, Francesca Zambon
Funding acquisition: Matteo Massironi, Federico Tosi
Investigation: Gloria Tognon
Methodology: Gloria Tognon, Francesca Zambon, Cristian Carli
Project administration: Matteo Massironi, Federico Tosi
Supervision: Matteo Massironi

Integrated Spectral and Compositional Analysis for the Lunar Tsiolkovskiy Crater

Gloria Tognon[1,2] , Francesca Zambon[3] , Cristian Carli[3] , Matteo Massironi[1,2,4] , Lorenza Giacomini[3] , Riccardo Pozzobon[4] , Giulia Salari[3] , Federico Tosi[3] , Jean-Philippe Combe[5], and Sergio Fonte[3]

[1]Centro di Ateneo di Studi e Attività Spaziali "G. Colombo", Università degli Studi di Padova, Padua, Italy, [2]Istituto Nazionale di Astrofisica - Osservatorio Astronomico di Padova (INAF-OAPd), Padua, Italy, [3]Istituto Nazionale di Astrofisica - Istituto di Astrofisica e Planetologia Spaziali (INAF-IAPS), Rome, Italy, [4]Dipartimento di Geoscienze, Università degli Studi di Padova, Padua, Italy, [5]Planetary Science Institute, Tucson, AZ, USA

Abstract Remote sensing observations represent the primary means in the production of geologic maps of planetary surfaces. However, they do not provide the same level of detail as Earth's geologic maps, which rely also on field observations and laboratory analyses. Color-derived basemaps can help to bridge this gap by highlighting peculiar surface and compositional properties. Here, we analyzed the spectral properties of the lunar Tsiolkovskiy crater through the definition of spectral units summarizing the information enclosed by a set of selected spectral parameters. We then performed a compositional analysis of the newly derived spectral units that helped us in discriminating the presence and relative abundance of the main mineralogical phases on the Moon. As a final step, we produced a geo-stratigraphic map of the Tsiolkovskiy crater integrating in a single mapping product both morphologic, stratigraphic and compositional information. The basaltic infilling of the crater is distinguished by three spectral units associated with distinct effusive events presenting a different composition. On the central peak, plagioclase and olivine suggest the presence of Mg-suite rocks from the lower crust. The continuous ejecta deposits are mostly characterized by impact melts and shocked materials rich in glass or agglutinates related to more mature terrains from which occasionally appear fresher anorthositic and gabbroic outcrops exposed by the inward sliding of the crater walls. Overall, the geo-stratigraphic map allows inferring compositional variations associated with the different morpho-stratigraphic units, which clarify and elaborate on the compositional heterogeneities within the lunar crust and the Tsiolkovskiy crater, and its geologic evolutionary history.

Plain Language Summary The main data used to produce geologic maps of planetary surfaces come from orbiting missions. However, geologic maps of Earth provide much more information, relying also on observations made on the field and analyses made in the laboratory. Color images derived from the combination and processing of spectral information can help to make planetary maps more comprehensive, similarly to the Earth's ones, by drawing attention to surface and compositional aspects. In this work, we performed a spectral and compositional study of the Tsiolkovskiy crater on the Moon which enabled us to distinguish the presence and relative quantity of the most common minerals constituting the lunar rocks. We also produced a geo-stratigraphic map coupling the information about the surface textures and shapes, relative time of deposition, and composition. On the basaltic floor, we discriminated the presence of three different spectral characteristics correlated with a sequence of flooding events showing distinct properties and a central peak exhibiting rocks emerged from the lowest strata of the lunar crust. The continuous ejecta blanket, instead, is characterized by mature materials interspersed by fresher exposures of subsurface materials. To conclude, the new mapping product allows an in-depth interpretation of the geologic evolution of the Tsiolkovskiy crater.

1. Introduction

Over the last few years, the renewed interest in robotic and human space exploration has made it even more evident that planetary morpho-stratigraphic maps alone do not provide the same level of information as the Earth's geologic maps. On Earth, unlike other planetary bodies, the possibility of performing in situ observations of the bedrock and collecting samples allows the production of comprehensive geologic maps coupling remotely sensed data with ground-truth observations and laboratory analyses.

To fill in this information gap, the most effective solution is the integration of morpho-stratigraphic maps with spectral data and derived products, such as color-derived basemaps (e.g., false colors, color ratios, principal

Validation: Gloria Tognon, Francesca Zambon
Visualization: Gloria Tognon
Writing – original draft: Gloria Tognon
Writing – review & editing: Gloria Tognon, Francesca Zambon, Cristian Carli, Matteo Massironi, Lorenza Giacomini, Riccardo Pozzobon, Giulia Salari, Federico Tosi

components, spectral indices) returning compositional and mineralogical information, to produce planetary maps as comprehensive as possible, similar to terrestrial ones. In past years, attempts at data integration have been performed on Daedalia Planum on Mars (Giacomini et al., 2012), and on Mercury in the Rembrandt basin (Semenzato et al., 2020), the H06-Kuiper quadrangle (Giacomini et al., 2021), and the H05-Hokusai quadrangle (Wright et al., 2024).

According to these authors, the integration with spectral and compositional data can be achieved following two different interpretative approaches, namely the contextual and in-series ones (Massironi et al., 2021). The first approach includes the production of two different maps based on monochrome and color-derived imagery, respectively (Semenzato et al., 2020). As a result, the spectral contacts defined by color variations may significantly diverge from contacts defined by morphology. Instead, the in-series approach includes the improvement of a morpho-stratigraphic map through the integration of spectral and color information. The final result is a map in which geologic boundaries may be slightly modified and morpho-stratigraphic units are subdivided into subunits according to color variations (e.g., Giacomini et al., 2012; Wright et al., 2024). The final product is, in both cases, a map integrating morphological and spectral information.

Regarding the Moon, a recent study by Tognon et al. (2021) performed a contextual integration between the photo-interpretation of the surface morphology and the compositional information derived from multispectral color data for the Tsiolkovskiy crater, a Late Imbrian complex crater about 200 km in diameter formed by a NW-SE oblique impact (Whitford-Stark, 1982) on the far side. The integration of compositional information was performed based on color variations from the Clementine UVVIS Warped Color Ratio mosaic (R: 750/415 nm; G: 750/1,000 nm; B: 415/750 nm) (Lucey et al., 2000) generated using three of the six spectral filters of the Clementine Wide Angle UVVIS camera (McEwen & Robinson, 1997; Nozette et al., 1994). On the basaltic mare covering Tsiolkovskiy's floor, in particular, the geologic study highlighted the presence of distinct flooding events characterized by a different color hue reflecting distinct composition and age. Crater size-frequency distribution measurements revealed that at least three consecutive effusive events took place within Tsiolkovskiy in a span of about 690 Ma. The effusions were characterized by yellow (average ratios of 750/415 nm and 750/1,000 nm), purple-blue (higher 415/750 nm ratio) and orange (higher 750/415 nm ratio) hues and were correlated to the oldest (3.6 Ga), intermediate (3.4 Ga) and youngest (2.9 Ga) event, respectively. Of the three, the bluer color of the midway event was interpreted to indicate the effusion of lavas characterized by higher amounts of TiO_2 with respect to the previous flooding event, as also confirmed by the Lunar Reconnaissance Orbiter (LRO) Wide Angle Camera (WAC)-derived titanium abundance estimation map (Sato et al., 2017), thus suggesting an evolution of the magmatic source over time. Beyond the mare flooded floor, the dark blue and cyan Clementine color hues dispersed on the inner slope, central peak and hummocky floor of Tsiolkovskiy were interpreted as exposures of norites and anorthosites less affected by space weathering with respect to the surrounding red reworked highland material (Heather & Dunkin, 2002; Pieters & Tompkins, 1999).

Here we further investigated the spectral and compositional properties of the lunar Tsiolkovskiy crater through the creation and analysis of a Spectral Units (SUs) map based on hyperspectral Moon Mineralogy Mapper (M^3) data. The definition of SUs, indeed, is a reliable method that helps summarize the information enclosed by a set of selected spectral parameters by processing them simultaneously (Zambon et al., 2022). We then used the SUs map to create a new geo-stratigraphic map of our study area, namely a more comprehensive mapping product integrating the previously published morpho-stratigraphic map (Tognon et al., 2021) with the spectral information derived from the M^3 data. We finally compared the SUs' reflectance spectra with those of laboratory studies to obtain more information on the compositional and mineralogical properties of the materials exposed within the Tsiolkovskiy crater and thus on their geological evolution.

2. Datasets and Processing Methods

2.1. Datasets

Data used for producing the Spectral Units map were acquired by the Chandrayaan-1/Moon Mineralogy Mapper (M^3) instrument (Goswami & Annadurai, 2008; Pieters et al., 2009), which collected the most comprehensive hyperspectral dataset available for the Moon. M^3 was an imaging spectrometer covering the visible to near-infrared (420–3,000 nm) spectral range acquiring data in two operational modes, that is, the global and target mode. The global mode achieved a spatial resolution of about 140 m/px and a spectral sampling of 20 or 40 nm over 86 of the available 260 spectral channels, whereas the target mode collected data with a spatial resolution of

about 80 m/px and a spectral sampling of 10 nm over all the 260 channels. This observational strategy allowed for a detailed mineralogical characterization of the lunar surface. Given the lack of targeting data for the Tsiolkovskiy crater, for this work we used reflectance data acquired in global mode, thereafter calibrated and photometrically corrected (Green et al., 2011; Besse et al., 2013a, 2013b).

To produce a geo-stratigraphic map integrating the geological and spectral information of our study area, we then used the publicly available GIS shapefile data from the morpho-stratigraphic and color-based spectral (hereafter Clementine-based) maps of Tsiolkovskiy crater (Tognon et al., 2021) (Figures 1a–1c), together with the newly M[3]-derived SUs map (Figure 1d). As a reference, we also used the LRO-WAC monochrome (Robinson et al., 2010) and Clementine UVVIS Warped Color Ratio (Lucey et al., 2000) mosaics, with a scale of about 100 and 200 m/px respectively, and the Lunar Orbiter Laser Altimeter (LOLA) and Kaguya Terrain Camera Digital Elevation Model (DEM) (Barker et al., 2016), providing the elevation data with a horizontal scale of about 59 m/px and a vertical accuracy of 3–4 m, from which it was derived a topographic hillshade (Tognon et al., 2021).

2.2. Processing Methods

2.2.1. Spectral Units Map

Moon spectra are characterized by steep spectral slopes (i.e., increase in reflectance with increasing wavelength) and show two large absorption bands centered at 1,000 and 2,000 nm respectively. The shape and wavelength position of these bands mostly depend on the presence of large cations (Fe^{2+}, Ca^{2+}, and Mg^{2+}) occupying the octahedral M1 and M2 sites in the crystallographic structure of pyroxenes and olivine (Burns, 1993), or in glassy materials (e.g., Adams & McCord, 1971; Tompkins & Pieters, 2010). In comparable spectral ranges, another relevant mineralogical phase presenting an absorption due to the presence of Fe^{2+} is chromite, belonging to the spinel group (Cloutis et al., 2004). Regarding the steepness of lunar spectral slopes, this is caused by the interaction between the surface material and the space environment. Space weathering, indeed, strongly affects the airless surface of the Moon causing the formation and accumulation of submicroscopic metallic iron ($smFe^0$) particles that lead to the darkening and reddening of the optical spectrum (e.g., Pieters & Noble, 2016; Tai Udovicic et al., 2021). As a result, a surface exposed to space weathering processes for a longer period of time will have a higher degree of maturity and a steeper "redder" spectrum (e.g., Denevi et al., 2023; Fischer & Pieters, 1994; Kumar & Kumar, 2014).

We settled on four of the most representative spectral parameters helpful in enhancing the compositional variations on the Moon and, specifically, within the Tsiolkovskiy crater. The same parameters were considered for the spectral analysis of the Apollo and Von Karmàn basins (Zambon et al., 2021). In particular, we selected (a) the reflectance at 540 nm (R540), (b) the band depth at 1,000 nm (BDI), (c) the band depth at 2,000 nm (BDII), and (d) the spectral slope between 540 nm and the maximum of the first and second shoulder of the BDI (SSBI).

The R540 is a standard visible wavelength used to discuss reflectance differences. It helps in discriminating variations in composition, maturity degree, surface roughness and grain size between different materials (Clark, 1999; Cloutis et al., 1986; Sharkey et al., 2021). High reflectance values are indeed associated with the lunar plagioclase highlands and bright and newly exposed materials. On the contrary, the dark basaltic maria composed of a larger number of mafic and opaque mineralogical phases show low reflectance values. Moreover, reflectance is inversely proportional to grain sizes and surface roughness variations.

The BDI and BDII parameters, calculated according to Clark and Roush (1984), highlight variations in the abundance of opaque materials and primary mineralogical phases (e.g., pyroxenes, olivine and plagioclase) and of grain size (Clark, 1999; Sharkey et al., 2021). In this case, higher concentrations of pyroxenes, and olivine (limited to BDI), produce deeper absorption bands whereas, as for the R540 value, the band depth values decrease with prolonged exposure to space weathering.

Finally, the SSBI index, calculated according to Cuzzi et al. (2009) and Filacchione et al. (2012), evidences compositional differences along with terrain maturity and grain size variations (Clark, 1999). In particular, high spectral slope values are associated with older terrains presenting a higher degree of maturity while younger terrains and darker terrains show low spectral slope values.

Starting from the selected parameters, the method of extrapolation and definition of the SUs follows the work by Zambon et al. (2022) for the H05-Hokusai quadrangle on Mercury.

Geologic units
Crater floor units
- sm Smooth material
- hm Hummocky material
- cp Central peak

Crater wall units
- sp Smooth ponds
- ss Steep scarps
- is Inner slope

Geologic contacts
— Contact, certain

Linear features
— Crest of small crater rim D<1km
— Crest of large crater rim D>20km
— Mare rille
— Fault, certain
--- Fault, uncertain
— Wrinkle ridge

R750/415 nm | R750/1000 nm | R415/750 nm

Clementine-based units
- bp1 Basaltic plain 1
- bp2 Basaltic plain 2
- bp3 Basaltic plain 3
- nt Noritic-anorthosite/troctolite
- Anorthosite
- ns Mature and reworked highland soil

Spectral contacts
--- Contact, approximate
— Contact, certain

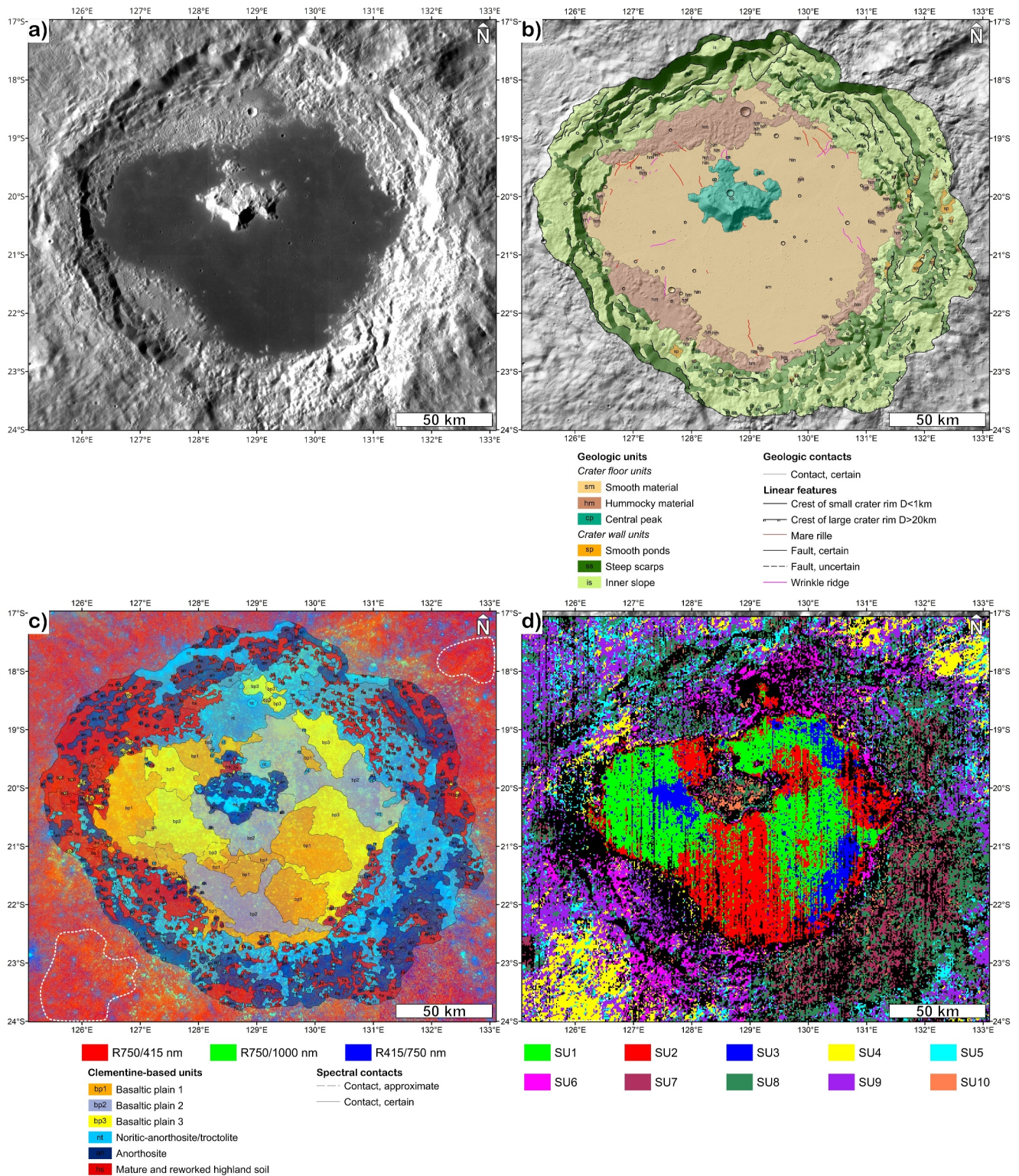SU1 | SU2 | SU3 | SU4 | SU5
SU6 | SU7 | SU8 | SU9 | SU10

Figure 1.

For each spectral index, we considered its histogram distribution and divided the range of values into five to six threshold intervals (from low to high/very high values) depending on the statistical parameters (i.e., mean, mode, median, standard deviation) of the histogram distribution and on the 2D density scatter plot of the spectral parameter. Figure 2 shows the thresholding of the R540 parameter while the Supporting Information S1 is a full overview of the histograms, scatter plots and threshold interval maps for all the spectral parameters. All defined threshold intervals were then intermingled, and all unique combinations resulted in distinct Spectral Units. We merged units with similar spectral index values (<10%) and excluded the sparsely populated ones (i.e., number of pixels <10^5). As a result, we obtained a Spectral Units map with ten SUs conveying the spectral information fulfilled by all the spectral indices (Figure 1d).

2.2.2. Compositional Investigation

To thoroughly investigate the compositional properties of the Tsiolkovskiy crater, we considered the reflectance spectra associated with each SU. We also processed the spectra by removing the continuum through the application of a second degree polynomial fitting and of a linear fitting for the band center at 1,000 nm and 2,000 nm, respectively, and considering the 580–770 nm and 1,400–1,469 nm range of wavelengths for the bands shoulders.

We then compared the SUs' average reflectance spectra with laboratory spectra of lunar rock-forming materials and, in particular, those of synthetic pyroxenes from the NASA Reflectance Experiment LABoratory (RELAB) database (Klima et al., 2011a, 2011b). Pyroxenes, indeed, are the most common mafic minerals on the Moon (e.g., Lucey, 2004), occurring predominantly in the basaltic maria but also across the lunar highlands. Besides being the dominant mafic minerals on the Moon, pyroxenes represent a valuable tool for understanding the lunar crustal and magmatic evolution (e.g., Pieters et al., 2006). Their crystallographic structure and composition provide us insights into their magmatic source and the lunar thermal evolution. As previously said, the lunar spectra exhibit two major near-infrared absorption bands centered around 1000 (BCI) and 2000 (BCII) nm, respectively, which are spectrally typical of pyroxenes. Specifically, the abundance of Fe^{2+} and Ca^{2+} in pyroxenes causes a shift of BCI and BCII toward longer wavelengths. Similar behavior, however, can be associated with the presence of other mineralogical phases, such as olivine, plagioclase and spinel (i.e., chromite), or glasses. Depending on their composition, indeed, the presence of large cations can cause a shift of the BCI and BCII to longer wavelengths for olivine and chromite, respectively, a longer-wavelength shift of both BCI and BCII for plagioclase, and a greater shift of the BCI rather than the BCII in glassy materials (Gaffey, 1976; Klima et al., 2007, 2011b).

Starting from the continuum-removed spectra, we derived the band centers as the band minimum fitted by a second degree polynomial (Cloutis et al., 1986). We then plotted BCI versus BCII and compared the results with those of the synthetic pyroxenes by Klima et al. (2011a, 2011b).

Finally, for estimating the relative abundance of pyroxene and olivine, likely abundant in the lunar mantle and fundamental for understanding its evolution (e.g., Yamamoto et al., 2010), we calculated the Band Area Ratio (BAR), namely the ratio between the 2,000 and 1,000 nm absorption bands' areas. By plotting the BCI versus BAR value, we compared our results to those of the olivine-pyroxene mixtures trend by Cloutis et al. (1986), recently modified by Gaffey et al. (1993) and Pieters et al. (2005) and recently reworked by Zhang & Cloutis (2021a, 2021b).

2.2.3. Mapping Data Fusion

We produced our geo-stratigraphic map by integrating Tsiolkovskiy's morpho-stratigraphic map (Tognon et al., 2021) with the spectral information derived from the SUs map, taking into consideration the preliminary spectral information inferred from the Clementine-based map. Figure 1 shows the input data for the data fusion. To perform the data merging following an in-series approach, we used the Esri ArcMap 10.4.1 software and a mapping scale of 1:400,000.

Figure 1. Input basemaps for mapping data fusion. (a) Lunar Reconnaissance Orbiter Wide Angle Camera monochrome global mosaic (up to 100 m/px) in equirectangular projection (Robinson et al., 2010). (b) Morpho-stratigraphic map visualized on top of the Digital Elevation Model-derived hillshade with 50% transparency, modified from Tognon et al. (2021). (c) Clementine-based spectral map visualized on top of the Clementine UVVIS Warped Color Ratio mosaic (up to 200 m/px; Lucey et al., 2000) with 50% transparency, modified from Tognon et al. (2021); the white dashed lines delimit areas corresponding to the SU4 and SU5. (d) M^3-derived Spectral Units map; the black color refers to unclassified pixels.
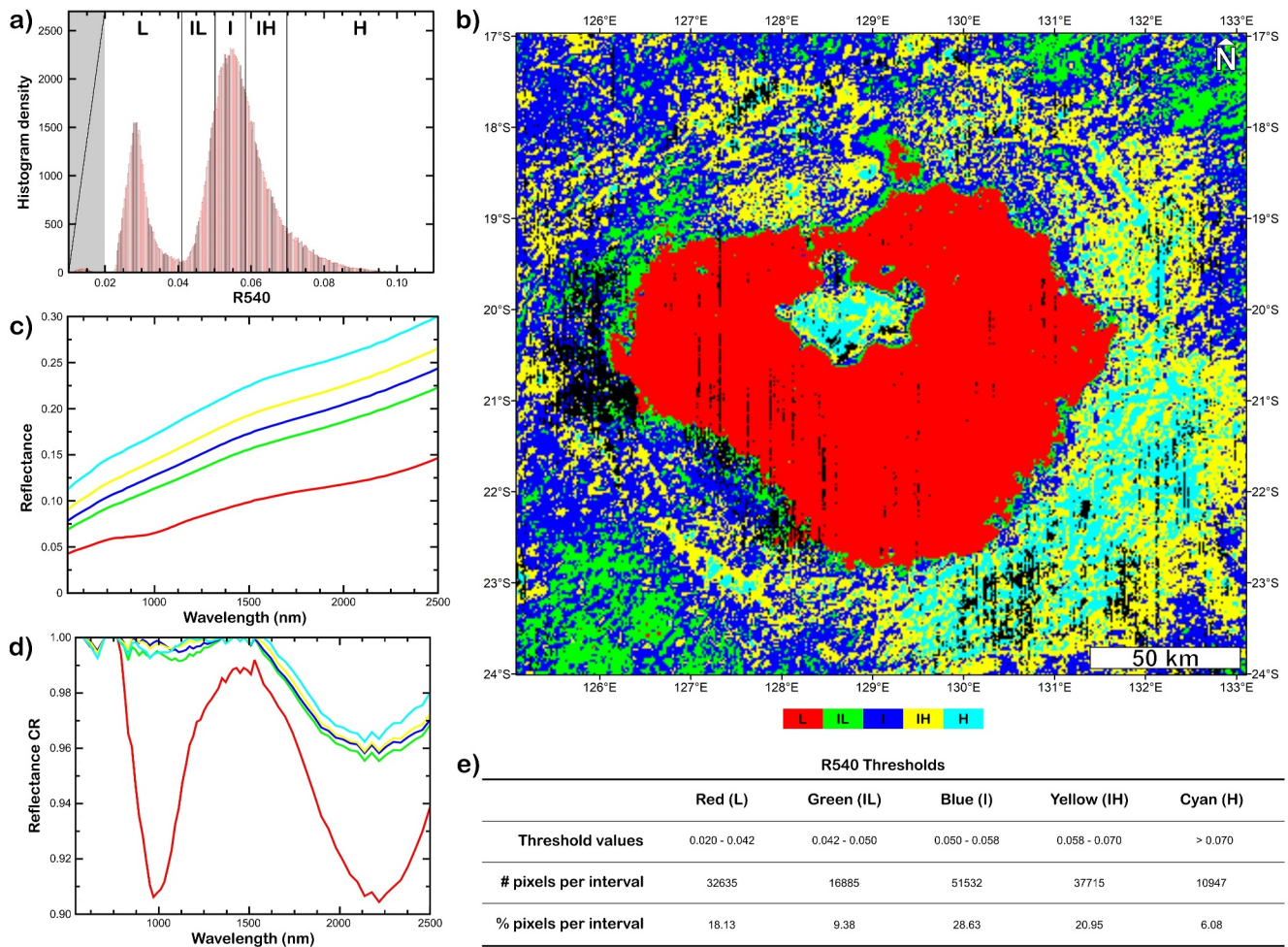
Figure 2. Spectral index thresholding: example for the R540 parameter. (a) Histogram distribution; black lines delimit the threshold intervals in low (L), intermediate-low (IL), intermediate (I), intermediate-high (IH) and high (H) values. (b) Map with threshold classes (each color refers to a specific interval from low to high values). (c) Average reflectance spectra and (d) continuum removed spectra for each threshold class. (e) Threshold values table. See the Supporting Information S1 for a full overview of the histograms, scatter plots and threshold interval maps for all spectral parameters.

As a starting point, we imported the linear contacts digitalized for the Clementine-based map and modified them to define the boundaries between the different spectral units in the SUs map. This was particularly useful in the digitalization of contacts in unclassified terrains that in the SUs map are represented by black areas. We then imported the geologic contacts from the morpho-stratigraphic map and superposed them on the newly defined contacts to produce a mapping linework integrating the spectral and geological information. In particular, we observed that spectral contacts can (i) overlap or (ii) intersect a morpho-stratigraphic contact, or (iii) lie within a morpho-stratigraphic unit (Tognon et al., 2021). In the first case, the spectral contact matches a geologic one thus indicating a boundary between both distinct morpho-stratigraphic and spectral units. Consequently, we removed the spectral contact in favor of the morpho-stratigraphic contact, digitized on a much higher spatial resolution basemap. The morpho-stratigraphic unit will be then characterized by a single spectral signature representing the homogeneity from a compositional point of view of that unit. In the case of a spectral contact intersecting a geologic one, we interpreted this relationship as the result of a peculiar spectral characteristic affecting more than one morpho-stratigraphic unit, such as a pre-impact contact between different bedrock lithologies or a talus deposit covering the substratum and having the same composition as the scarp they detached from. When the spectral contact lies within a morpho-stratigraphic unit (case iii), it can (i) close on the geologic contact, or (ii) isolate a portion of the geologic unit highlighting, in both cases, the presence of a distinct spectral behavior.
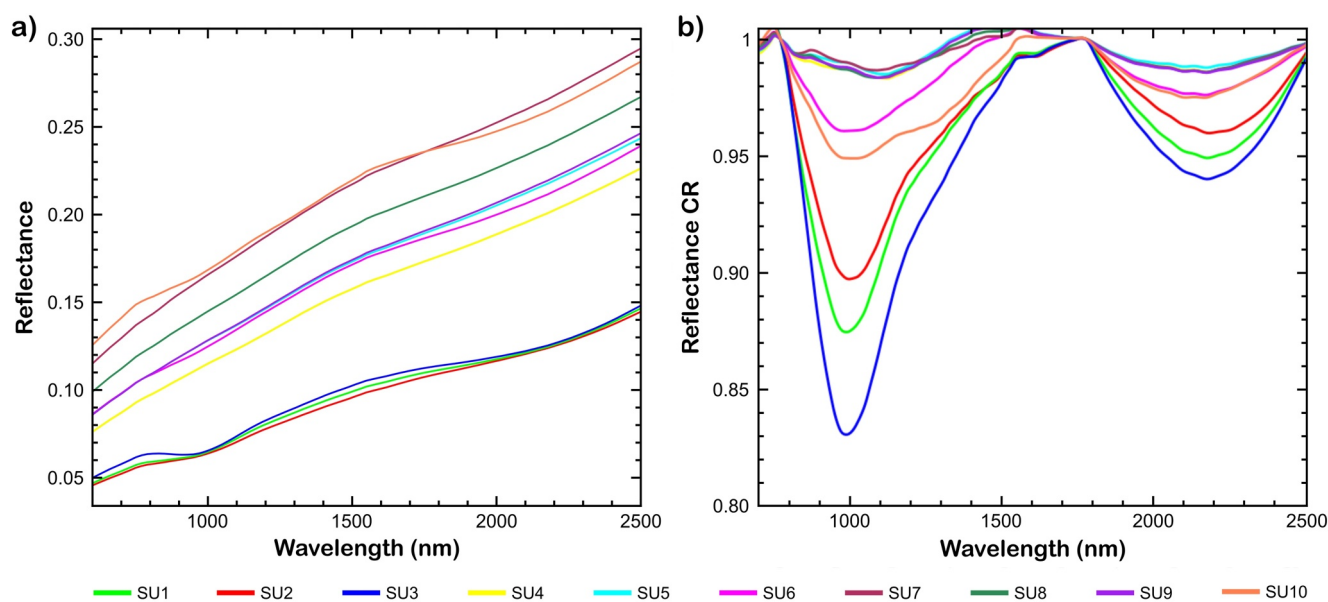
Figure 3. Reflectance spectra for our Spectral Units. (a) Average reflectance spectra of the SUs. (b) Same as (a) with continuum removal. Colors of the spectra are consistent with the SU colors displayed in Figure 1d.

In the integrated mapping product, we used black and white lines for the morpho-stratigraphic and spectral contacts respectively. We then employed these contacts to create new geo-stratigraphic units, resulting from the integration of geologic and spectral information, whose names derive from the combination of the original morpho-stratigraphic unit name (i.e., *sm*, *hm*, *cp*, *sp*, *ss*, *is* units; Tognon et al., 2021) followed by the spectral unit number (e.g., *smSU1*). We used a similar strategy for the units' color scheme, attributing to each SU a different hue while maintaining the same color scheme as from the morpho-stratigraphic map. The remaining morpho-logical and tectonic linear features (e.g., mare rilles, faults, etc.) were imported, as from the morpho-stratigraphic map, and overlaid on the final product.

3. Results

3.1. Compositional Analysis

From the reflectance spectra of our SUs (Figure 3), we observe that the SU1, SU2 and SU3 stand out for presenting the lowest (i.e., bluer) spectral slopes and the strongest absorptions around 1,000 and 2,100–2,200 nm with respect to the other SUs. Shallower absorption bands characterize the spectral trends of the SU6 and SU10. Of the two, the SU6 shows intermediate reflectance values likely reflecting the presence of Fe-bearing miner-alogical phases and of glasses. Inversely, the high reflectance spectrum of the SU10 possibly reflects a significant contribution of plagioclase as indicated also by the presence of an absorption at about 1,300 nm (Horgan et al., 2014). The remaining spectral units (i.e., SU4, SU5, SU7, SU8 and SU9) present different spectral slopes but very weak absorption bands both at 1,000 and 2,100–2,200 nm, with slight differences in spectral shape and position of absorption bands especially around 900–1,400 nm. Compared to the SU1, SU2, SU3, SU6, and SU10, this behavior reflects differences in mineralogy and a higher contribution of space weathering, which contributes to the formation of agglutinates (e.g., Pieters & Noble, 2016).

The differences in the spectra for our SUs can be described with the spectra of synthetic pyroxenes (Klima et al., 2011a, 2011b). The scatter plot in Figure 4a shows the spectral variability within the range of 1,000 and 2,000 nm band centers of orthopyroxenes (Ca-free pyroxenes) and clinopyroxenes, namely pigeonites (low-Ca pyroxenes) and augites (high-Ca pyroxenes), characterized by a different abundance of wollastonite (Wo), enstatite (En) and ferrosilite (Fs) components. In the same plot, we displayed the average derived BCI and BCII of our SUs.

The SU1, SU2, SU3, SU6, SU7 and the SU10 cluster in between the low-Ca pigeonitic (i.e., Wo_{5-20}) and the high-Ca augitic (i.e., Wo_{20-45}) groups, thus ruling out the presence of orthopyroxene and suggesting a low to
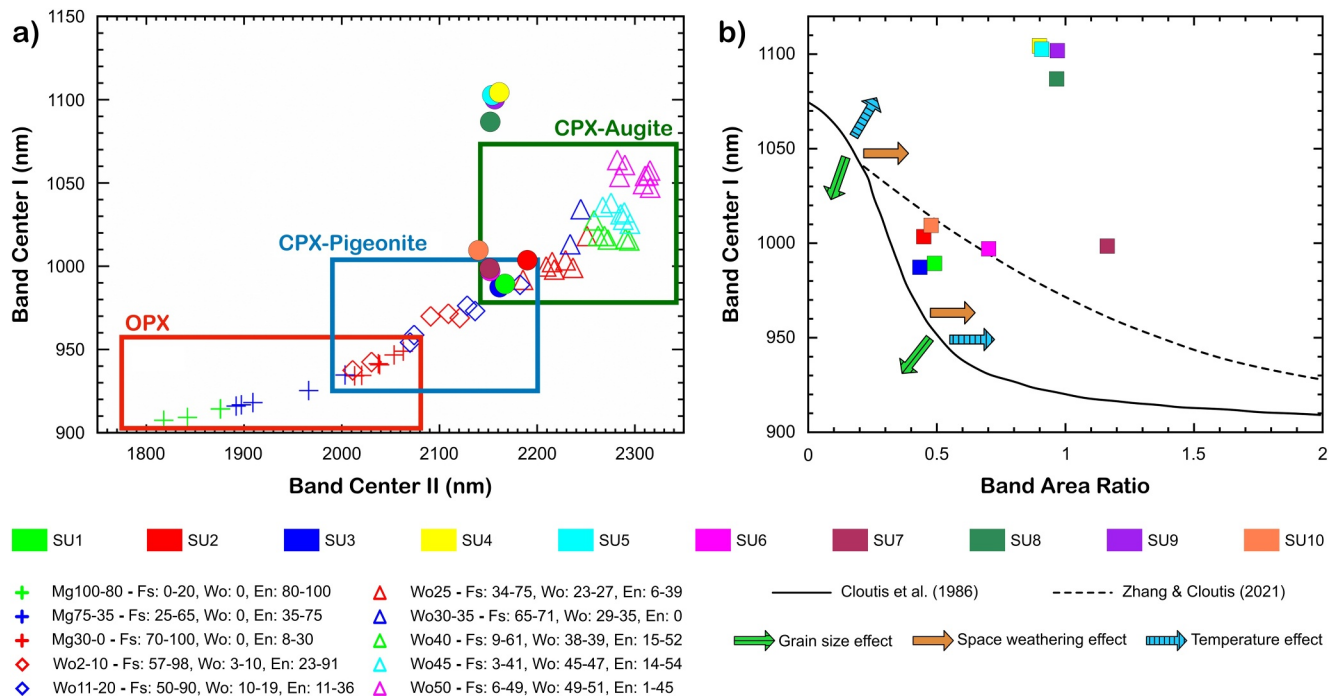
Figure 4. Scatter plots for the compositional analysis of Tsiolkovskiy crater. (a) Average derived band centers for Ca-free (OPX, plus), low-Ca (CPX-Pigeonite, diamonds) and high-Ca (CPX-Augite, triangles) synthetic pyroxenes (Klima et al., 2011a, 2011b) and for our SUs (full circles) plotted within the range of 1,000 nm (Band Center I) and 2,000 nm (Band Center II). Refer to the legend for color interpretation of the SUs and the different abundances of wollastonite (Wo), enstatite (En) and ferrosilite (Fs) considered within the OPX and CPX groups. (b) Average derived band centers at 1,000 nm plotted versus the Band Area Ratio parameter. Refer to the legend for color interpretation. The black straight line refers to the olivine-orthopyroxene mixtures trend by Cloutis et al. (1986) and the black dashed line refers to the olivine-clinopyroxene-orthopyroxene mixtures trend by Zhang & Cloutis (2021a). The colored arrows indicate the influence of grain size, space weathering and temperature effects on the trend, as from Pieters et al. (2005).

intermediate Ca^{2+} content ($\sim$20%) and relatively high Fe^{2+} content in clinopyroxene. Notably, all these units, with the exception of the SU7, also present the strongest absorption bands. The remaining SUs, namely the SU4, SU5, SU8 and SU9, instead, do not fall inside a defined pyroxene group. Although they display BCII values similar to the other SUs, these units present a notable shift of BCI toward longer wavelengths. Consistent with laboratory studies, the displacement of BCI could reflect an increase in the Fe^{2+}/Ca^{2+} content in pyroxenes (Gaffey, 1976; Klima et al., 2007, 2011a), but it should be followed by an increasing BCII. However, it could also reflect variations in the abundance of a different mineralogical phases such as spinel, plagioclase, and olivine, or due to a higher abundance of glasses. Such mineralogical phases, as well as glasses, are mainly characterized by a stronger absorption centered around 1,000–1,300 nm with a negligible, or absent, band close to 2,000 nm. An exception is represented by spinel that, depending on composition, could have absorptions at 2,000 nm toward longer wavelengths.

To investigate whether olivine could be the major responsible for the BCI shift toward longer wavelengths, we plotted BCI versus BAR (Figure 4b), following the method applied, for example, by Beck et al. (2011) and Carli et al. (2018), on meteorite samples. We also superimposed the results on the olivine-orthopyroxene and olivine-clinopyroxene-orthopyroxene mixture trends by Cloutis et al. (1986) and Zhang & Cloutis (2021a, 2021b) respectively. Being characterized by a broad asymmetric absorption band near 1,000 nm and no absorption at 2,000 nm (Burns, 1993), the dunitic (>90wt% of olivine) end-member region lies around BCI values of 1,050 nm and very low (<0.3) BAR. Considering also the information derived from the BCI versus BCII plot, the analysis of the BCI versus BAR plot can help us infer more about the composition of the different SUs.

The SU1, SU2 and SU3, characterized by a pigeonitic (i.e., SU1 and SU3) to augitic (i.e., SU2) composition, show a similar BAR value (i.e., 0.5). The SU2, moreover, shows a shift of BCI toward longer wavelengths that may be associated with an increase in Ca^{2+} content in clinopyroxenes (Cloutis, 2002; Klima et al., 2011a) or with a relative enrichment of olivine, plagioclase, and spinel, or of glasses. Similar behavior characterizes the SU10,

showing BAR and BCI values similar to the ones of the SU2. However, the shift toward shorter wavelengths of BCII for the SU10, indicating a more pigeonitic composition compared to the SU1 and SU3, ought to imply a corresponding shift of BCI and thus a lower BAR value. The centering of BCI toward longer wavelengths therefore could suggest the involvement of another mafic phase contributing at 1,000 nm and not at 2,000 nm. In this case, the relatively deep absorption bands of the SU10 and the shift toward shorter wavelengths of BCII seem to exclude both the contribution of glass and spinel (e.g., chromite), which would result in a decrease of the BAR and a shift of BCII toward longer wavelengths, respectively (Cloutis et al., 2004). Hence, olivine and plagioclase could be the most likely mineralogical phases contributing to the shift of BCI toward longer wavelengths. As previously stated, the SU10 shows the highest average reflectance spectrum and an absorption around 1,300 nm possibly reflecting a significant contribution of plagioclase, even cumulitic. At the same time, the closeness of this spectral unit to the olivine-clinopyroxene-orthopyroxene mixing trend (Zhang & Cloutis, 2021a) (Figure 4b) could indicate the presence, in small amounts, of olivine. Both hypotheses may suggest an anorthositic (or leuco-gabbroic) or troctolitic composition depending on the relative abundances of plagioclase and olivine, which seems to contrast with the detection of purest anorthosite (Lemelin et al., 2015; Ohtake et al., 2009) and support the presence of olivine (Corley et al., 2018; Pieters et al., 1996).

The SU6 and SU7 show a BCI intermediate between the SU1 and SU2 and a BCII intermediate between the SU10 and SU3. However, their BAR value is greater than those associated with the SU1, SU2, SU3, and SU10. This increase is due to the shallower absorption bands of the spectra, more evident in the SU7, and likely indicating the contribution of opaque mineralogical phases and glasses, progressively increasing from the SU6 to the SU7. At the same time, the high average reflectance spectra of the SU7 could imply an increase in the abundance of plagioclase.

Concerning the isolated cluster formed by the SU4, SU5, SU8, and SU9, the increase of both BCI and BAR values excludes the presence of olivine. The evidence of faint absorption bands at 1,000 and 2,000 nm, on the other hand, still indicates the involvement of mafic mineralogical phases yet glasses very likely mask their contribution.

3.2. Geo-Stratigraphic Map

By integrating the spectral and compositional information returned by the SUs map and the previous geologic knowledge (i.e., from the morpho-stratigraphic map), the integrated geo-stratigraphic map of the lunar Tsiolkovskiy crater (Figure 5; see the Main Map and related information in Supporting Informations S2 and S3) allows a more thorough interpretation of the geology of the basin. To have a more straightforward overview of the spatial distribution of our SUs, in Figure 6 we present a number of diagrams showing the distribution of each SU across the whole Tsiolkovskiy basin as well as within each geologic unit.

In the following sections, we describe our main morpho-stratigraphic units, putting emphasis on their compositional analysis and interpretation of origin and formation. In support, Table 1 provides a brief description of the units identified by Tognon et al. (2021) in their morpho-stratigraphic and Clementine-based spectral maps.

3.2.1. Crater Floor, Smooth Material (sm)

Whereas most of the SUs show a somewhat scattered distribution among the different geologic units, the SU1, SU2 and SU3 are the only SUs completely enclosed and describing the *sm* unit and no other morpho-stratigraphic unit. Nevertheless, these spectral units seem fairly well correlated with the distribution of the *bp1*, *bp2* and *bp3* units from the Clementine-based map, respectively, confirming yet again the presence of three distinct basaltic flooding events and, consequently, a correlation to a specific age and compositional variation (Tognon et al., 2021).

Specifically, the SU3 correlates well with the oldest (~3.6 Ga) *bp3* unit, showing intermediate values of Clementine-derived ratios of 750/415 and 750/1,000 nm. This false-color is a result of the longer exposure of this unit to space weathering, causing the formation of agglutinates (i.e., a combination of minerals and glasses) and the alteration of mineral FeO into smFe^0. The correlation of the SU3 to the oldest lava flowing event is finally reflected by the low surface area extent of this spectral unit (see Figure 6a), which was covered by subsequent flooding events.

Consecutively to the SU3, the SU2 shows a major correlation with the *bp2* unit, the intermediate effusive event occurred around 3.4 Ga and characterized by a high 415/750 nm Clementine color ratio, interpreted as the result of
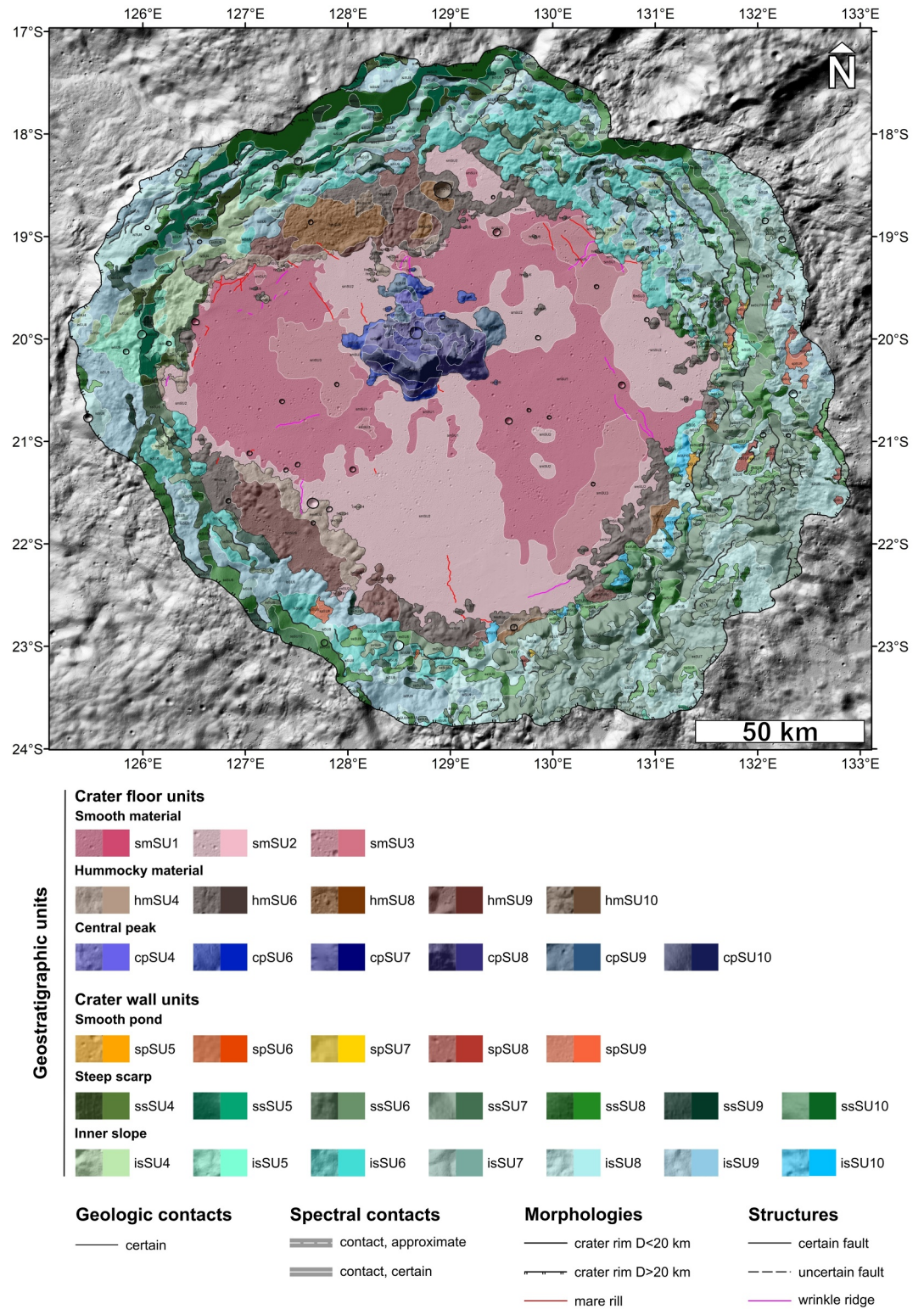
Figure 5. Geo-stratigraphic map of the Tsiolkovskiy crater visualized on top of the Digital Elevation Model-derived hillshade with 50% transparency. Refer to the legend for color interpretation. See the Main Map in Supporting Informations S2 and S3.
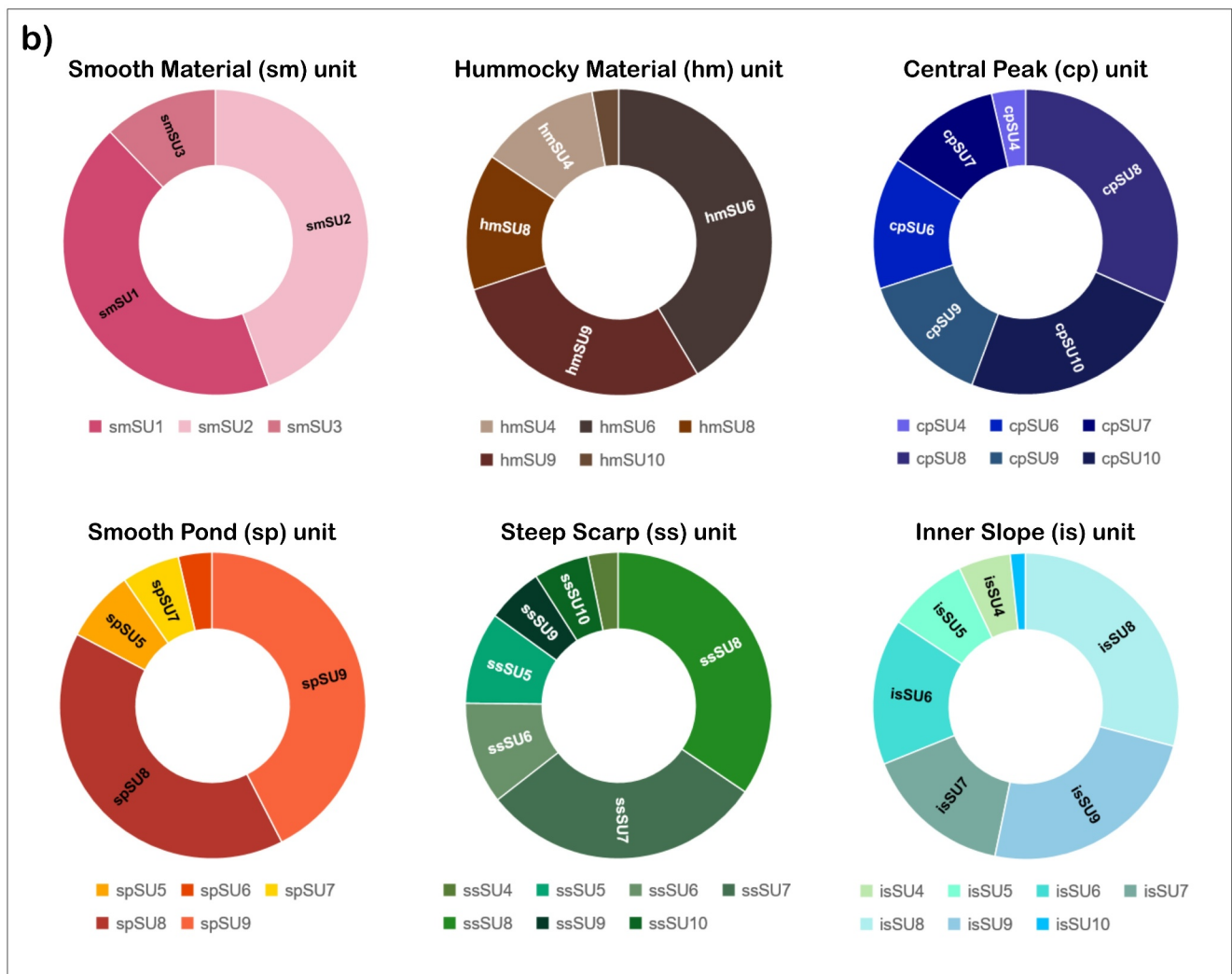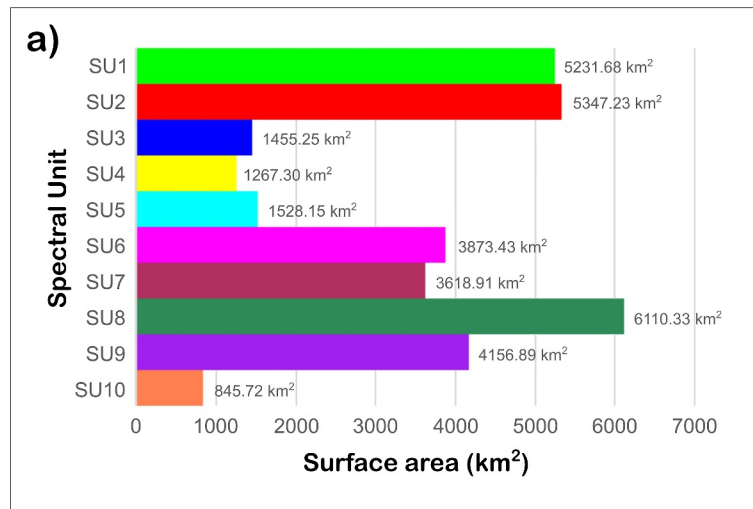
Figure 6. Spatial distribution of the Spectral Units. (a) Histogram bar of the total surface area occupied by each SU, listed in ascending order. Refer to Figure 1d for color interpretation. (b) Pie charts indicating the internal percentage distribution between the different SUs per morpho-stratigraphic unit. Refer to Figure 5 for color interpretation.

Table 1
List of Units Identified in the Previously Published Morpho-Stratigraphic and Clementine-Based Spectral Maps for Tsiolkovskiy Crater by Tognon et al. (2021)

Morpho-stratigraphic map	
Geologic units	Unit description
Smooth material – *sm*	Smooth and dark mare deposit sparsely cratered presenting sharp boundaries with respect to adjacent materials
Hummocky material – *hm*	Pre-mare material reworked during the impact characterized by an irregular and rough surface with rounded hills
Central peak – *cp*	Well-preserved morphology standing out from the surrounding dark crater floor
Smooth ponds – *sp*	Localized smooth areas of impact melt scattered on the crater rim
Steep scarps – *ss*	Steep scarps with slopes >40° exposed by collapses of the crater rim
Inner slope – *is*	Terraces and scarps <40° generated by the inward collapse of the crater rim
Clementine-based spectral map	
Clementine-based spectral units	Unit description
Basaltic plain 1 – *bp1*	Localized younger lava emplacements characterized by a higher R750/R415 nm ratio
Basaltic plain 2 – *bp2*	Intermediate events of lava emplacements characterized by a higher R415/R750 nm ratio and a relative enrichment in TiO_2 content (Sato et al., 2017)
Basaltic plain 3 – *bp3*	Older lava emplacements characterized by average R750/R415 ratios and R750/R1000 nm reflect the high concentration of mafic minerals long exposed to space weathering
Noritic-anorthosite/troctolite – *nt*	Unit characterized by average ratios of R750/R1000 and R415/R750 nm reflecting the presence of lithologies with minor amounts of Fe-bearing minerals (e.g. norite, troctolite)
Anorthosite – *an*	Anorthosite-rich lithologies characterized by a bright albedo and high R415/R750 nm ratio
Mature and reworked highland soil – *hs*	Highland soil enriched in glass content indicative of surface maturation caused by space weathering and characterized by high R750/R415 nm ratio

Note. For each unit, we provide a short description according to the authors.

an increase in the concentration of TiO_2 (Tognon et al., 2021). This change in composition is also highlighted by the spectrum of this SU, which presents the lowest average reflectance and the shallower absorption bands when compared to the SU1 and SU3. Furthermore, the compositional analysis highlights that, of the three spectral units located on the smooth floor, the SU2 shows a shift of both BCI and BCII toward longer wavelengths (see Figure 4a), indicating a change toward a more augitic (high-Ca clinopyroxene) composition with respect to the SU1 and SU3.

The youngest (~2.9 Ga) flooding event, corresponding to the Clementine-based *bp1* unit and characterized by a high 750/415 nm color ratio, finally, is mostly correlated with the SU1. Contrary to the SU2, this unit shows a more pigeonitic (low-Ca clinopyroxene) composition, similar to the SU3, suggesting a depletion of the material causing the enrichment in TiO_2 and Ca^{2+} during the previous lava flowing event.

3.2.2. Crater Floor, Hummocky Material (hm)

From Figure 6b, we can observe that the composition of the hummocky floor material of Tsiolkovskiy is described for the most part by the SU6. Its shallow absorption bands and intermediate reflectance spectrum suggest the presence of Fe-bearing minerals and of glasses, as we would expect from the impact melt material constituting this morpho-stratigraphic unit. Overall, the composition of the SU6 correlates well with the association of this spectral unit to Clementine-based *hs* and *nt* units, representing weathered highland soil material and gabbroic rocks, respectively.

The remaining spectral units characterizing the *hm* unit correspond to the SU9, SU8, SU4, and SU10 (in decreasing order of internal percentage distribution). The SU9, SU8, and SU4, in particular, show a discordant behavior due to a great shift of BCI toward longer wavelengths (see Figure 4). Their absorption spectra, however, still show very shallow absorptions at 1,000 and 2,000 nm that do not exclude the presence of mafic mineralogical phases. The behavior of these units most likely reflects the strong contribution of glasses, consistent with the impact melt origin of the hummocky floor material. On the other hand, the SU10 exhibits the highest reflectance
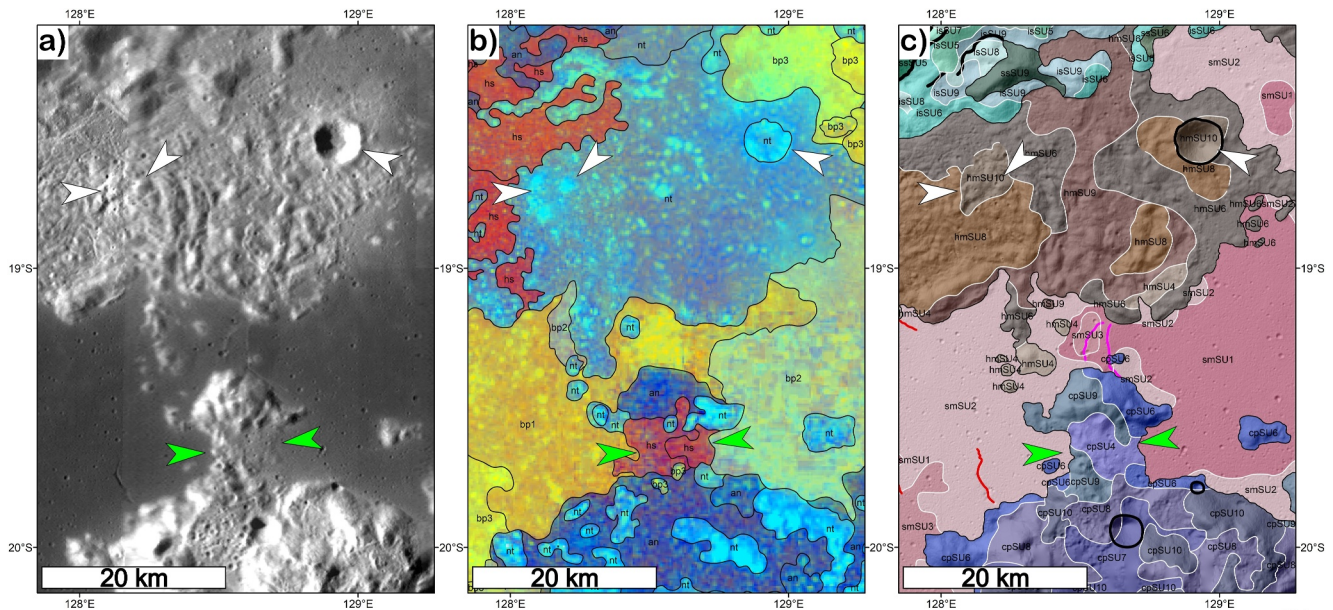
Figure 7. Detailed views from the (a) Lunar Reconnaissance Orbiter Wide-Angle Camera monochrome mosaic (Robinson et al., 2010), (b) Clementine-based map (Tognon et al., 2021) visualized on top of the Clementine UVVIS Warped Color Ratio mosaic (Lucey et al., 2000) with 50% transparency, and c) geo-stratigraphic map. The white arrows point to a patch of bright material (to the NW) and a superimposing crater (to the NE) associated with the *hmSU10* unit; the green arrows point to the neck area of the central peak associated with the *cpSU4* unit. Refer to Figures 1c and 5 for linework and units' interpretation.

spectrum, as well as a different spectral shape around 1,300 nm, and it possibly reflects the presence of plagioclase. In fact, this spectral unit matches with a superimposing impact crater and a patch of brighter material, both located on the northern hummocky plains (see Figure 7, white arrows), which might be the result of the excavation and deposition of brighter and fresher underlying materials with respect to the weathered and glass-rich impact melts of the *hm* unit.

3.2.3. Crater Floor, Central Peak (cp)

Compared to the other morpho-stratigraphic units, the SU10 shows its maximum surface area distribution on the central peak of the Tsiolkovskiy crater. The high abundance of plagioclase seems to be a likely contributor to the high average reflectance spectrum of this spectral unit, which is most likely only barely affected by space weathering. Similarly, the BCI versus BAR plot may highlight the contribution of small amounts of olivine and thus of a more troctolitic composition. Hence, the straightforward association of the SU10 with the Clementine-based *nt* unit well suits the presence of troctolitic anorthosites.

With a shift of BCI toward long wavelengths, the SU4 in the central peak reflects the strong contribution of weathered materials and glasses. This is also highlighted by the correspondence of this spectral unit to the Clementine-based *hs* unit (see Figure 7, green arrows), indicating the presence of mature highland soil material, which is circumscribed on the roughly textured neck area connecting the main central peak morphology to its northern high-standing bulges.

Also, the SU6, SU7, SU8, and SU9 reflect a glass-dominated composition. On the other hand, they also present intermediate-to-high reflectance spectra that likely indicate the contribution of plagioclase, even cumulitic, as also suggested by the correlation of these spectral units with the *nt* and *an* Clementine-based units. The high reflectance spectra of the SU7 and SU8 seem to suggest plagioclase as a major component of these spectral units compared to pyroxene, likely reflecting the presence of anorthositic gabbros to gabbroic anorthosites. Finally, the limited spatial distribution of the SU6 and SU9 on the margins and lower elevation areas of the *cp* unit might reflect, in terms of composition, the onlap contact of the basaltic infilling on the steep slopes of the central peak and thus explain the major content in mafic mineralogical phases of these two spectral units with respect to the other SUs characterizing the *cp* unit, indicating thus the presence of gabbroic rocks.

3.2.4. Crater Wall, Smooth Ponds (sp)

All the spectral units associated with the geologic *sp* unit (i.e., SU9, SU8, SU5, SU7, and SU6 in decreasing order of percentage distribution) show a clear correlation with the *hs* unit. The association with this Clementine-based unit and the results of the compositional analysis highlight that these spectral units reflect the presence of mature highland soil material characterized by a high glass content due to prolonged exposure to space weathering processes.

3.2.5. Crater Wall, Steep Scarps (ss)

SU4, SU5, SU6, SU7, SU8, SU9, and SU10 characterize the composition of the steep scarp material. Most of these spectral units reflect a composition strongly dominated by glasses. This is not surprising if we consider that the material constituting the steep scarps is space-weathered highland soil reworked by the impact and successively exposed during the post-cratering modification stage.

Considering the oblique impact origin of the Tsiolkovskiy crater, we can observe that the SE downrange direction inferred by Whitford-Stark ([1982](#)) is predominantly associated with the SU7. Together with the SU6, SU8, and SU9, these spectral units, associated with the Clementine-based *nt* and *an* units, show intermediate-to-high average reflectance spectra reflecting the contribution of plagioclase, which characterizes the partially exposed fresher (with respect to the inner slope material) walls of the crater. In the case of the SU7 and SU8, plagioclase seems a major contributor compared to other mineralogical phases, suggesting for these two spectral units a more anorthositic composition (i.e., anorthositic gabbros to gabbroic anorthosites) with respect to the SU6 and SU9 (i.e., gabbros). A similar composition characterizes the SU10 that, as for the central peak morphology, is enriched in plagioclase, which together with small amounts of olivine indicate the presence of troctolitic anorthosites.

On the other hand, the uprange portion of the crater sees the largest distribution of SU4 and SU5. These spectral units, not presenting peculiar absorptions nor outstanding reflectance spectra, cover a pretty small surface area with respect to other non-mare spectral units (Figure [6a](#)). Looking at larger patches of SU4 and SU5 located outside the NE and SW margins of Tsiolkovskiy's rim and comparing them with the Clementine UVVIS Color Ratio mosaic (see Figure [1c](#), white dashed lines), we observe that they seem very well correlated with the presence of mature highland soil, confirming once again the intergrow of crystalline and amorphous material characterizing the spectral properties of both the SU4 and SU5. Besides, the strong presence of agglutinates on these fresher steep scarps might reflect the contamination of more mature material collapsed from the inner slope, thus masking the presence of gabbroic rocks.

3.2.6. Crater Wall, Inner Slope (is)

The inner slope of Tsiolkovskiy, similar to the *ss* unit, is described by all SUs except for the three SUs correlated with the basaltic mare (i.e., SU1, SU2, and SU3). This indicates that the material composing the inner walls of the crater has a composition comparable to the *ss* unit with a higher degree of maturity, being mostly deposited on relatively stable terraces. This is also pointed out by the correlation of the *is* morpho-stratigraphic unit with the *hs* Clementine-based unit, associated with space-weathered highland material enriched in agglutinates.

Different from the steep scarps, where the inward collapse of the crater rim led to the exposure of fresher walls of anorthosite, the inner slope is made up of shocked materials excavated by the impact and melted materials accumulated under the influence of gravity on terraces and depressions. In this instance, the high glass content causing the shift of BCI toward longer wavelengths for the SU8 and SU9 and the high BAR value of the SU7 takes on a greater importance, indicating the presence of impact melts. Likewise, the plagioclase-rich SU10 may be an indication of polymictic breccias made up even of large anorthositic clasts.

The SU6, as previously stated, reflects the presence of mafic minerals and glasses that correlate well with impact melt materials ejected during the impact. This is even more evident for the SU4 and SU5 that, as in the case of the steep scarps, show a strong correlation with the mature highland soil and thus to agglutinates-rich materials.

4. Discussions

The compositional information derived from M^3 data provides a better understanding of the lithologies present in our study area. Even though the Clementine UVVIS Color Ratio mosaic helped in yielding a first insight into it,

allowing a preliminary distinction of mare and highland material, the lower resolution of the data prevented a broad categorization of the rock types within the Tsiolkovskiy crater. Results obtained from the compositional investigation of the M³-derived SUs were used to determine the presence and relative abundance of the main mineralogical phases on the Moon, namely plagioclase, pyroxene and olivine. Through the ternary classification diagrams of the plagioclase-pyroxene-olivine and plagioclase-orthopyroxene-clinopyroxene systems (Stöffler et al., 1980), we were able to associate each SU with a predominant lithology.

The dark floor material defined by the SU1, SU2 and SU3 characterized by low reflectance values and strong absorption bands, caused by the sizable amount of iron-bearing mineralogical phases (e.g., pyroxenes and olivine) masking the contribution of other, less absorber phases (e.g., plagioclase; Horgan et al., 2014), indicate the presence of basaltic rocks characterized by very low (i.e., <1 wt% TiO_2) to low (i.e., 1–5 wt% TiO_2) titanium values (Taylor et al., 1991). The contribution of plagioclase seems only to determine an increase in albedo in plagioclase-bearing lithologies (Anbazhagan & Arivazhagan, 2009) and affect their average reflectance slopes. This is well demonstrated by the high reflectance spectra of the SU7, SU8, and SU10, the latter presenting also an absorption band at 1,300 nm indicative of the strong contribution of plagioclase (Horgan et al., 2014). While the SU7 and SU8 reflect the presence of anorthositic gabbros to gabbroic anorthosites, depending on the relative abundance of plagioclase and clinopyroxene, the detection of olivine for the SU10 well supports the presence of troctolitic anorthosites as suggested by Pieters et al. (1996) and Corley et al. (2018). In between, the SU4, SU5, SU6, and SU9 are characterized by intermediate reflectance spectra and faint absorption bands, with the exception of the SU6 indicating a major contribution of iron-bearing phases, and they likely reflect the presence of gabbros sensu stricto. Norites are not mentioned because the compositional investigation returned no correlation between any SUs and the presence of orthopyroxene, one of the main mineralogical phases constituting this lithology.

Overall, these lithologies are characteristic of the rock types making up the Mg-suite (e.g., Norman & Ryder, 1980; Shearer & Papike, 2005; Wieczorek et al., 2006) and well fit the localization of Tsiolkovskiy crater on the extensive and highly anorthositic lunar region known as Feldspathic Highlands Terrane (Jolliff et al., 2000), an area including most of the lunar far side and characterized by heavy cratering, sparse maria, and elevated crustal thickness (Wieczorek et al., 2013).

Overall, the geologic evolution of our study area can be summarized as follows. Around 3.6 Ga, a NW-SE low-angle impact on the lunar far side led to the formation of the ∼200 km in diameter Tsiolkovskiy crater. The impact occurred on a highly anorthositic crust with an average thickness of 40–45 km and it is likely to have exhumed material from a depth of up to 30 km (Cintala & Grieve, 1993; Tompkins & Pieters, 1999) thus sampling the more mafic materials (e.g., troctolites, gabbros) constituting the lower lunar crust. As represented in Figure 8a, indeed, the pre-impact crust was likely consisting of an upper crust of anorthosite interspersed by pockets of gabbroic rocks and a lower crust of purer anorthosite containing intrusions of olivine-bearing materials (e.g., troctolite). The high crustal thickness and the lack of detection of orthopyroxene likely rule out the exposure of upper mantle material which should bear a detectable amount of orthopyroxene (Moriarty et al., 2021).

The oblique impact caused the excavation of highlands material and its fragmentation, shock and melting. This is particularly evident in the SE downrange direction where, due to the oblique impact origin of the crater, the ejecta distribution displays a preferential concentration. The hummocky floor, smooth ponds and inner slope material, indeed, show a preferential spatial distribution on the downrange portion of the crater. Furthermore, from the compositional analysis they reflect a significant contribution of glasses (e.g., *isSU8*, *isSU9*, *isSU7*, *hmSU6*, *hmSU9*, etc., in decreasing order of surface area) masking the presence of plagioclase (e.g., *isSU10*) and, likely, of other mineralogical phases (e.g., *hmSU6*, *isSU6*). Overall, the glass-enriched composition well suits the presence of impact melts and breccias of the ejecta deposits or agglutinates related to more mature terrains.

The rebound of the crust during the modification stage led to the formation of the central peak and the inward collapse of the crater's inner wall caused the formation of terraces and scarps. In detail, the central peak of Tsiolkovskiy is in large part characterized by the SU10 (i.e., *cpSU10*), which shows its maximum distribution in this morpho-stratigraphic unit. As seen from the compositional analysis, the high average reflectance values and the shift of BCI toward longer wavelengths for the SU10 support the presence of plagioclase and olivine respectively. Their presence suggests a troctolitic composition, with likely small amounts of olivine, typical of the Mg-suite rocks constituting the lower crust (Taylor et al., 1993), indicating thus that the central peak was not able to exhume material from the mantle, most likely located too far beneath the lunar highlands, but at least to sample the troctolitic intrusions located within the lower crust (see Figure 8a). Even though masked by glasses, also the
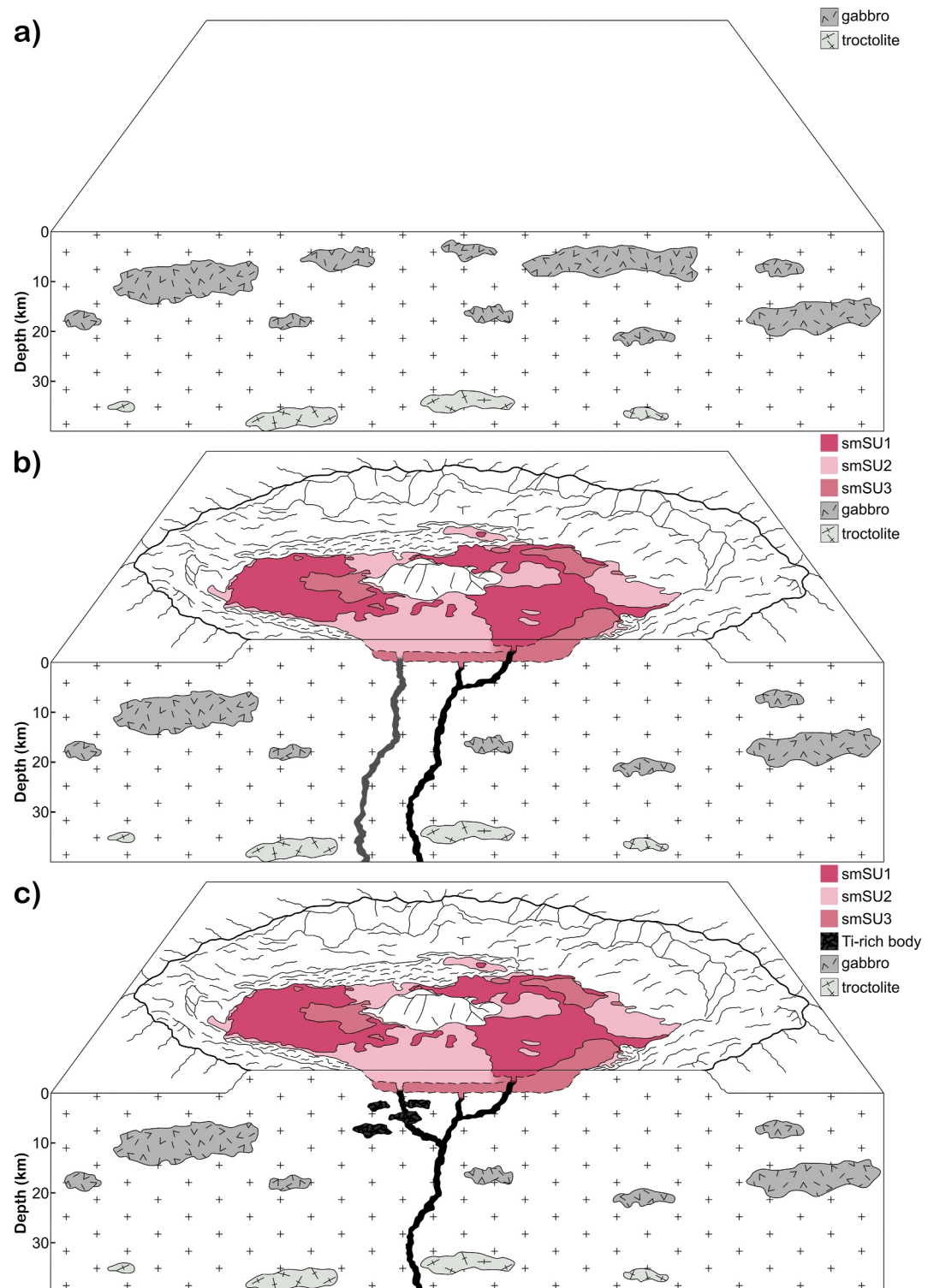
Figure 8. Schematic representation of the putative crustal stratigraphy in the area of the Tsiolkovskiy crater. a) Pre-impact crust consisting of a highly anorthositic upper crust interspersed by gabbroic bodies and a lower crust of purer anorthosite containing intrusions of troctolite. b) Post-impact crust representing two distinct magma sources feeding the *smSU3/smSU1* and *smSU2* units, respectively, the latter fed by Ti-enriched magmas. c) Post-impact crust representing the same magma source feeding both the *smSU3/smSU1* and *smSU2* units; during magma rising, the *smSU2* unit assimilates Ti-rich bodies within the crust.

remaining spectral units characterizing the central peak (i.e., *cpSU8*, *cpSU9*, *cpSU6*, and *cpSU7* units, in decreasing order of internal percentage distribution), with the only exception of the *cpSU4* unit associated with a hummocky area of mature highland material, indicate the contribution of plagioclase, as also suggested by the Clementine Color Ratio mosaic.

A similar compositional interpretation can be applied to the crater's steep scarps. During the modification stage, the inner walls of the transient crater slid inward leading to the formation of steep scarps interspersed by terraces covered by impact melt material. In this case as well, indeed, glasses mask the contribution of other mineralogical phases. Nonetheless, as for the central peak morphology, the *ssSU8*, *ssSU7*, *ssSU6*, *ssSU9*, and *ssSU10* units (in decreasing order of internal percentage distribution) reflect the presence of plagioclase indicating the exposure of the "fresher" anorthositic bedrock. The presence of glasses can be attributed equally to the slumping of more mature material from the inner slope terraces, the progressive maturation of the exposed scarp material, and/or the deposition of distal ejecta from nearby craters.

For what concerns the smooth mare of Tsiolkovskiy, in the 700 Ma following the impact, three different effusive events took place favored by impact-generated fractures acting as conduits for magma rising. The identification of spectral units located within the mare infilling (i.e., SU1, SU2, and SU3) allowed for a more defined internal subdivision of the smooth plains with respect to the Clementine-based spectral map. The effusive events correspond to the *smSU1*, *smSU2*, and *smSU3* units representing the youngest (around 2.9 Ga), intermediate (around 3.4 Ga) and oldest (>3.6 Ga) events respectively, so that the numerical order reflects the stratigraphic order. These units are also fairly well correlated with the *bp1* (higher 750/415 nm ratio), *bp2* (higher 415/750 nm ratio) and *bp3* (average ratios of 750/415 nm and 750/1,000 nm) Clementine-based units respectively. The compositional analysis, furthermore, highlights that to the pigeonitic composition of the *smSU3* unit followed an increase in the Ca^{2+} content in pyroxenes, also associated with enrichment in TiO_2 content, for the *smSU2* unit progressively depleted during the latest *smSU1* event. The high-Ca and Ti-bearing mineralogical phases of the *smSU2* unit indicate a substantial change in magmatism occurred between the oldest and intermediate effusive events. These elements, indeed, are usually more abundant in basalts derived by an initial and limited melting of the mantle sources or, alternatively, by crustal assimilation processes. Hence the occurrence of these enrichments with respect to the *smSU3* unit might be related to a limited partial melting of a distinct magma source (see Figure 8b) or to the assimilation of ilmenite-bearing bodies within the crust during magma rising (see Figure 8c).

5. Conclusions

Compared to the previous mapping products (Tognon et al., 2021), the integrated geo-stratigraphic map presented in this work allows for a more comprehensive interpretation of the geologic evolution within the lunar farside Tsiolkovskiy crater by enclosing in a single mapping product both morphologic, stratigraphic and compositional information. We analyzed the spectral properties of the study area through an M^3-derived Spectral Units map (see Zambon et al., 2022) useful in highlighting the compositional properties. The retrieval of reflectance spectra, band centers and BAR values for the SUs and their comparison with laboratory data allowed inferring the presence and abundance of mineralogical phases (e.g., plagioclase, olivine, pyroxene, opaques) or glasses and the relative abundance of Mg^{2+}, Fe^{2+}, and Ca^{2+} cations within pyroxenes. The composition returned by each SU was then interpreted case by case according to the morpho-stratigraphic unit under consideration so that a specific spectral unit could be associated with a different lithology and rock origin. For instance, when considered within the *ss* and *is* geologic units, the SU10 is associated with anorthositic bedrock and polymictic breccias, respectively. This apparent discrepancy reflects the much broader geologic interpretation that can be performed when spectral and compositional information are available in supporting of geology.

This geological mapping approach allowed us to infer the following outstanding facts about Tsiolkovskiy's geologic context and evolution.

1. The impact leading to the formation of the Tsiolkovskiy crater occurred on an anorthositic-dominated crust characterized by scattered pockets of gabbroic rocks and troctolites.
2. The central peak of Tsiolkovskiy is characterized by a strong contribution of plagioclase with small amounts of olivine, indicating isolated intrusions of olivine-dominated material (i.e., troctolite) in the lower crust.
3. The Tsiolkovskiy crater's walls show variable contents of Ca-pyroxene and plagioclase, suggesting a highly anorthositic upper crust punctuated by gabbroic intrusions.

4. The impact exhumed material from a depth of up to ∼30 km (i.e., lower crust) but it was not able to exhume material from the orthopyroxene-bearing upper mantle; indeed, no compositional correlation between the SUs and orthopyroxene was found, thus ruling out also the presence of norites.

5. The basaltic infilling covering the floor of the crater is more heterogeneous than expected for a relatively small mare such as Tsiolkovskiy's. While most SUs show no univocal geologic correlation, the mare is associated with three spectral units (i.e., SU1, SU2, and SU3) confirming once again the succession of three effusive events presenting a distinct composition and age.

6. The oldest (i.e., *smSU3*) and youngest (i.e., *smSU1*) flooding events consist of basalts with a more pigeonitic (i.e., low-Ca pyroxene) composition and low titanium contents, likely generated by the same magma source.

7. The intermediate effusive event (i.e., *smSU2*) shows an increased content in Ca^{2+} and TiO_2 with respect to the previous event, thus indicating a substantial change in magmatism; this change might be correlated to the assimilation of Ti-enriched intrusions located within the crust or to the partial melting of a distinct magma source.

To conclude, the new geo-stratigraphic map presented in this work takes a step forward in the thoroughness of the Moon's geologic maps, similar to Earth's ones. The definition of Spectral Units is a promising method for analyzing simultaneously different spectral parameters (e.g., reflectance, band depths, band centers, spectral slopes) and the compositional information that can be derived by comparing the obtained results with laboratory data represents a valuable resource for integrating planetary morpho-stratigraphic maps and better understanding the geological evolution of an area.

Data Availability Statement

The Moon Mineralogy Mapper data (Pieters et al., 2009) are publicly available in NASA's Planetary Data System (PDS) Cartography and Imaging Sciences Node (PDS, 2011). The Lunar Reconnaissance Orbiter Wide-Angle Camera monochrome global mosaic (Robinson et al., 2010), the Clementine UVVIS Warped Color Ratio global mosaic (Lucey et al., 2000), and the Lunar Orbiter Laser Altimeter and Kaguya Terrain Camera Digital Elevation Model (Barker et al., 2016) are publicly available in the U.S. Geological Survey (USGS) Astrogeology Science Center (USGS, 2008, 2013, 2015). The cartographic product presented in this work was produced using the ESRI ArcMap 10.4.1 software (ESRI, 2016). The figures shown in this work and the Main Map in Supporting Information S2 were assembled in Inkscape 1.2 (Inkscape, 2022). The geo-stratigraphic map is available online at https://doi.org/10.5281/zenodo.10423261 (Tognon et al., 2023a), with the GIS project, basemaps, mapping shapefiles, map sheet, and an explanatory "README.txt." Data used for the spectral analysis are available online at https://doi.org/10.5281/zenodo.10423459 (Tognon et al., 2023b).

References

Adams, J. B., & McCord, T. B. (1971). Optical properties of mineral separates, glass, and anorthositic fragments from Apollo mare samples. In *Proceedings of the second lunar science conference* (Vol. 3, pp. 2183–2195).

Anbazhagan, S., & Arivazhagan, S. (2009). Reflectance spectra of analog basalts; implications for remote sensing of lunar geology. *Planetary and Space Science*, *57*(12), 1346–1358. https://doi.org/10.1016/j.pss.2009.06.020

Barker, M. K., Mazarico, E., Neumann, G. A., Zuber, M. T., Haruyama, J., & Smith, D. E. (2016). A new lunar digital elevation model from the Lunar Orbiter Laser Altimeter and SELENE Terrain Camera. *Icarus*, *273*, 346–355. https://doi.org/10.1016/j.icarus.2015.07.039

Beck, P., Barrat, J. A., Grisolle, F., Quirico, E., Schmitt, B., Moynier, F., et al. (2011). NIR spectral trends of HED meteorites: Can we discriminate between the magmatic evolution, mechanical mixing and observation geometry effects? *Icarus*, *216*(2), 560–571. https://doi.org/10.1016/j.icarus.2011.09.015

Besse, S., Sunshine, J., Staid, M., Boardman, J., Pieters, C., Guasqui, P., et al. (2013a). A visible and near-infrared photometric correction for Moon Mineralogy Mapper (M3). *Icarus*, *222*(1), 229–242. https://doi.org/10.1016/j.icarus.2012.10.036

Besse, S., Yokota, Y., Boardman, J., Green, R., Haruyama, J., Isaacson, P., et al. (2013b). One Moon, many measurements 2: Photometric corrections. *Icarus*, *226*(1), 127–139. https://doi.org/10.1016/j.icarus.2013.05.009

Burns, R. G. (1993). *Mineralogical applications of crystal field theory* (2nd ed.). Cambridge University Press.

Carli, C., Pratesi, G., Moggi-Cecchi, V., Zambon, F., Capaccioni, F., & Santoro, S. (2018). Northwest Africa 6232: Visible–near infrared reflectance spectra variability of an olivine diogenite. *Meteoritics and Planetary Science*, *53*(10), 2228–2242. https://doi.org/10.1111/maps.13056

Cintala, M. J., & Grieve, R. A. F. (1993). Differential scaling: Implications for central structures in large lunar craters. In *Proceedings 14th lunar and planetary science conference* (pp. 291–292).

Clark, R. N. (1999). *Spectroscopy of rocks and minerals and principles of spectroscopy*. John Wiley & Sons.

Clark, R. N., & Roush, T. L. (1984). Reflectance spectroscopy: Quantitative analysis techniques for remote sensing applications. *Journal of Geophysical Research*, *89*(B7), 6329–6340. https://doi.org/10.1029/JB089iB07p06329

Cloutis, E. A. (2002). Pyroxene reflectance spectra: Minor absorption bands and effects of elemental substitutions. *Journal of Geophysical Research*, *107*(6), 6-1–6-12. https://doi.org/10.1029/2001je001590

Cloutis, E. A., Gaffey, M. J., Jackowski, T. L., & Reed, K. L. (1986). Calibrations of phase abundance, composition, and particle size distribution for olivine-orthopyroxene mixtures from reflectance spectra. *Journal of Geophysical Research*, *91*(B11), 11641–11653. https://doi.org/10.1029/jb091ib11p11641

Cloutis, E. A., Sunshine, J. M., & Morris, R. V. (2004). Spectral reflectance-compositional properties of spinels and chromites: Implications for planetary remote sensing and geothermometry. *Meteoritics and Planetary Science*, *39*(4), 545–565. https://doi.org/10.1111/j.1945-5100.2004.tb00918.x

Corley, L. M., McGovern, P. J., Kramer, G. Y., Lemelin, M., Trang, D., Gillis-Davis, J. J., et al. (2018). Olivine-bearing lithologies on the Moon: Constraints on origins and transport mechanisms from M3 spectroscopy, radiative transfer modeling, and GRAIL crustal thickness. *Icarus*, *300*, 287–304. https://doi.org/10.1016/j.icarus.2017.09.012

Cuzzi, J., Clark, R., Filacchione, G., French, R., Johnson, R., Marouf, E., & Spilker, L. (2009). Ring particle composition and size distribution. In M. K. Dougherty, L. W. Esposito, & S. M. Krimigis (Eds.), *Saturn from Cassini-Huygens* (pp. 459–509). Springer Netherlands. https://doi.org/10.1007/978-1-4020-9217-6_15

Denevi, B. W., Noble, S. K., Christoffersen, R., Thompson, M. S., Glotch, T. D., Blewett, D. T., et al. (2023). Space weathering at the Moon. *Reviews in Mineralogy and Geochemistry*, *89*(1), 611–650. https://doi.org/10.2138/rmg.2023.89.14

ESRI. (2016). ArcGIS desktop 10.4.1 [Software]. *Environmental Systems Research Institute*. Retrieved from https://www.esri.com/en-us/arcgis/products/arcgis-desktop/resources

Filacchione, G., Capaccioni, F., Ciarniello, M., Clark, R. N., Cuzzi, J. N., Nicholson, P. D., et al. (2012). Saturn's icy satellites and rings investigated by Cassini-VIMS: III - Radial compositional variability. *Icarus*, *220*(2), 1064–1096. https://doi.org/10.1016/j.icarus.2012.06.040

Fischer, E. M., & Pieters, C. M. (1994). Remote determination of exposure degree and iron concentration of lunar soils using VIS-NIR spectroscopic methods. *Icarus*, *111*(2), 475–488. https://doi.org/10.1006/icar.1994.1158

Gaffey, M. J. (1976). Spectral reflectance characteristics of the meteorite classes. *Journal of Geophysical Research*, *81*(5), 905–920. https://doi.org/10.1029/jb081i005p00905

Gaffey, M. J., Bell, J. F., Brown, R. H., Burbine, T. H., Piatek, J. L., Reed, K. L., & Chaky, D. A. (1993). Mineralogical variations within the S-type asteroid class. *Icarus*, *106*(2), 573–602. https://doi.org/10.1006/icar.1993.1194

Giacomini, L., Carli, C., Sgavetti, M., & Massironi, M. (2012). Spectral analysis and geological mapping of the Daedalia Planum lava field (Mars) using OMEGA data. *Icarus*, *220*(2), 679–693. https://doi.org/10.1016/j.icarus.2012.06.010

Giacomini, L., Carli, C., Zambon, F., Galluzzi, V., Ferrari, S., Massironi, M., et al. (2021). Integration between morphological and spectral characteristics for the geological map of Kuiper quadrangle (H06). *EGU General Assembly 2021*, 15052. https://doi.org/10.5194/egusphere-egu21-15052

Goswami, J. N., & Annadurai, M. (2008). Chandrayaan-1 mission to the Moon. *Acta Astronautica*, *63*(11–12), 1215–1220. https://doi.org/10.1016/j.actaastro.2008.05.013

Green, R. O., Pieters, C., Mouroulis, P., Eastwood, M., Boardman, J., Glavich, T., et al. (2011). The Moon Mineralogy Mapper (M3) imaging spectrometer for lunar science: Instrument description, calibration, on-orbit measurements, science data calibration and on-orbit validation. *Journal of Geophysical Research*, *116*(10), 1–31. https://doi.org/10.1029/2011JE003797

Heather, D. J., & Dunkin, S. K. (2002). Crustal stratigraphy of the Al-Khwarizmi-King/Tsiolkovsky-Stark region of the lunar farside as seen by Clementine. *Planetary and Space Science*, *50*(14–15), 1311–1321. https://doi.org/10.1016/S0032-0633(02)00125-3

Horgan, B. H. N., Cloutis, E. A., Mann, P., & Bell, J. F. (2014). Near-infrared spectra of ferrous mineral mixtures and methods for their identification in planetary surface spectra. *Icarus*, *234*, 132–154. https://doi.org/10.1016/j.icarus.2014.02.031

Inkscape. (2022). Inkscape 1.2 [Software]. *Inkscape Development Team*. Retrieved from https://inkscape.org/

Jolliff, B. L., Gillis, J. J., Haskin, L. A., Korotev, R. L., & Wieczorek, M. A. (2000). Major lunar crustal terranes: Surface expressions and crust-mantle origins. *Journal of Geophysical Research*, *105*(E2), 4197–4216. https://doi.org/10.1029/1999je001103

Klima, R. L., Dyar, M. D., & Pieters, C. M. (2011a). Near-infrared spectra of clinopyroxenes: Effects of calcium content and crystal structure. *Meteoritics and Planetary Science*, *46*(3), 379–395. https://doi.org/10.1111/j.1945-5100.2010.01158.x

Klima, R. L., Pieters, C. M., Boardman, J. W., Green, R. O., Head, J. W., Isaacson, P. J., et al. (2011b). New insights into lunar petrology: Distribution and composition of prominent low-Ca pyroxene exposures as observed by the Moon Mineralogy Mapper (M3). *Journal of Geophysical Research*, *116*(4), 1–13. https://doi.org/10.1029/2010JE003719

Klima, R. L., Pieters, C. M., & Dyar, M. D. (2007). Spectroscopy of synthetic Mg-Fe pyroxenes I: Spin-allowed and spin-forbidden crystal field bands in the visible and near-infrared. *Meteoritics and Planetary Science*, *42*(2), 235–253. https://doi.org/10.1111/j.1945-5100.2007.tb00230.x

Kumar, P. A., & Kumar, S. (2014). Estimation of optical maturity parameter for lunar soil characterization using Moon Mineralogy Mapper (M3). *Advances in Space Research*, *53*(12), 1694–1719. https://doi.org/10.1016/j.asr.2014.01.009

Lemelin, M., Lucey, P. G., Song, E., & Taylor, G. J. (2015). Lunar central peak mineralogy and iron content using the Kaguya Multiband Imager: Reassessment of the compositional structure of the lunar crust. *Journal of Geophysical Research: Planets*, *120*(5), 869–887. https://doi.org/10.1002/2014JE004778

Lucey, P. G. (2004). Mineral maps of the Moon. *Geophysical Research Letters*, *31*(8), 3–6. https://doi.org/10.1029/2003GL019406

Lucey, P. G., Blewett, D. T., Taylor, G. J., & Hawke, B. R. (2000). Imaging of lunar surface maturity. *Journal of Geophysical Research*, *105*(E8), 20377–20386. https://doi.org/10.1029/1999JE001110

Massironi, M., Rossi, A. P., Wright, J., Zambon, F., Poehler, C., Giacomini, L., et al. (2021). From morpho-stratigraphic to geo(spectro)-stratigraphic units: The PLANMAP contribution. *Annual meeting of Planetary Geologic Mappers, 2610*.

McEwen, A. S., & Robinson, M. S. (1997). Mapping of the Moon by clementine. *Advances in Space Research*, *19*(10), 1523–1533. https://doi.org/10.1016/S0273-1177(97)00365-7

Moriarty, D. P., Dygert, N., Valencia, S. N., Watkins, R. N., & Petro, N. E. (2021). The search for lunar mantle rocks exposed on the surface of the Moon. *Nature Communications*, *12*, 1–11. https://doi.org/10.1038/s41467-021-24626-3

Norman, M. D., & Ryder, G. (1980). Geochemical constraints on the igneous evolution of the lunar crust. In *Proceedings 11th lunar and planetary science conference* (pp. 317–331).

Nozette, S., Rustan, P., Pleasance, L. P., Horan, D. M., Regeon, P., Shoemaker, E. M., et al. (1994). The clementine mission to the Moon: Scientific overview. *Science*, *266*(5192), 1835–1839. https://doi.org/10.1126/science.266.5192.1835

Ohtake, M., Matsunaga, T., Haruyama, J., Yokota, Y., Morota, T., Honda, C., et al. (2009). The global distribution of pure anorthosite on the Moon. *Nature*, *461*(7261), 236–240. https://doi.org/10.1038/nature08317

PDS. (2011). Moon mineralogy mapper [Dataset]. *Planetary Data System, Cartography and Imaging Sciences Node*. Retrieved from https://pds-imaging.jpl.nasa.gov/volumes/m3.html

Pieters, C., Shkuratov, Y., Kaydash, V., Stankevich, D., & Taylor, L. (2006). Lunar soil characterization consortium analyses: Pyroxene and maturity estimates derived from Clementine image data. *Icarus*, *184*(1), 83–101. https://doi.org/10.1016/j.icarus.2006.04.013

Pieters, C. M., Binzel, R. P., Bogard, D., Hiroi, T., Mittlefehldt, D. W., Nyquist, L., et al. (2005). Asteroid-meteorite links: The Vesta conundrum (s). *Proceedings of the International Astronomical Union*, *1*(229), 273–288. https://doi.org/10.1017/S1743921305006794

Pieters, C. M., Boardman, J., Buratti, B., Chatterjee, A., Clark, R., Glavich, T., et al. (2009). The Moon mineralogy mapper (M3) on Chandrayaan-1. *Current Science*, *96*(4), 500–505.

Pieters, C. M., He, G., & Tompkins, S. (1996). Anorthosite and olivine layers of the farside upper crust at Tsiolkovsky. In *27th lunar and planetary science conference* (pp. 1035–1036).

Pieters, C. M., & Noble, S. K. (2016). Space weathering on airless bodies. *Journal of Geophysical Research: Planets*, *121*(10), 1865–1884. https://doi.org/10.1002/2016JE005128

Pieters, C. M., & Tompkins, S. (1999). Tsiolkovsky crater: A window into crustal processes on the lunar farside. *Journal of Geophysical Research*, *104*(E9), 21935–21949. https://doi.org/10.1029/1998JE001010

Robinson, M. S., Brylow, S. M., Tschimmel, M., Humm, D., Lawrence, S. J., Thomas, P. C., et al. (2010). Lunar Reconnaissance Orbiter Camera (LROC) instrument overview. *Space Science Reviews*, *150*(1–4), 81–124. https://doi.org/10.1007/s11214-010-9634-2

Sato, H., Robinson, M. S., Lawrence, S. J., Denevi, B. W., Hapke, B., Jolliff, B. L., & Hiesinger, H. (2017). Lunar mare TiO2 abundances estimated from UV/Vis reflectance. *Icarus*, *296*, 216–238. https://doi.org/10.1016/j.icarus.2017.06.013

Semenzato, A., Massironi, M., Ferrari, S., Galluzzi, V., Rothery, D. A., Pegg, D. L., et al. (2020). An integrated geologic map of the Rembrandt Basin, on Mercury, as a starting point for stratigraphic analysis. *Remote Sensing*, *12*(19), 3213. https://doi.org/10.3390/rs12193213

Sharkey, B. N. L., Reddy, V., Malhotra, R., Thirouin, A., Kuhn, O., Conrad, A., et al. (2021). Lunar-like silicate material forms the Earth quasi-satellite (469219) 2016 HO3 Kamoʻoalewa. *Communications Earth and Environment*, *2*(1), 231. https://doi.org/10.1038/s43247-021-00303-7

Shearer, C. K., & Papike, J. J. (2005). Early crustal building processes on the moon: Models for the petrogenesis of the magnesian suite. *Geochimica et Cosmochimica Acta*, *69*(13), 3445–3461. https://doi.org/10.1016/j.gca.2005.02.025

Stoffler, D., Knoll, H. D., Marvin, U. B., Simonds, C. H., & Warren, P. H. (1980). Recommended classification and nomenclature of lunar highland rocks - A committee report. In *Proceedings of the conference on the lunar highlands crust, Houston, Texas, November 14– 16, 1979* (pp. 51–70).

Tai Udovicic, C. J., Costello, E. S., Ghent, R. R., & Edwards, C. S. (2021). New constraints on the lunar optical space weathering rate. *Geophysical Research Letters*, *48*(14), 1–11. https://doi.org/10.1029/2020GL092198

Taylor, G. J., Warren, P., Ryder, G., Delano, J., Pieters, C. M., & Lofgren, G. (1991). Lunar rocks. In B. F, G. Heiken, & D. Vaniman (Eds.), *Lunar sourcebook, A user's guide to the Moon*. Cambridge University Press.

Taylor, S. R., Norman, M. D., & Esat, T. (1993). The lunar highland crust: The origin of the Mg suite. *Meteoritics*.

Tognon, G., Pozzobon, R., Massironi, M., & Ferrari, S. (2021). Geologic mapping and age determinations of Tsiolkovskiy crater. *Remote Sensing*, *13*(18), 3619. https://doi.org/10.3390/rs13183619

Tognon, G., Zambon, F., Carli, C., Massironi, M., Giacomini, L., Pozzobon, R., et al. (2023a). Geo-stratigraphic map of Tsiolkovskiy crater (Moon, Far side) [Dataset]. *Zenodo*. https://zenodo.org/records/10423261

Tognon, G., Zambon, F., Carli, C., Massironi, M., Giacomini, L., Pozzobon, R., et al. (2023b). Spectral units for Tsiolkovskiy crater (Moon, Far side) [Dataset]. *Zenodo*. https://zenodo.org/records/10423459

Tompkins, S., & Pieters, C. M. (1999). Mineralogy of the lunar crust: Results from Clementine. *Meteoritics and Planetary Science*, *34*(1), 25–41. https://doi.org/10.1111/j.1945-5100.1999.tb01729.x

Tompkins, S., & Pieters, C. M. (2010). Spectral characteristics of lunar impact melts and inferred mineralogy. *Meteoritics and Planetary Science*, *45*(7), 1152–1169. https://doi.org/10.1111/j.1945-5100.2010.01074.x

USGS. (2008). Clementine UVVIS warped color ratio mosaic [Dataset]. *U.S. Geological Survey, Astrogeology Science Center*. Retrieved from https://astrogeology.usgs.gov/search/map/moon_clementine_uvvis_warped_color_ratio_mosaic_200m

USGS. (2013). *Lunar Reconnaissance Orbiter Wide Angle Camera mosaic* [Dataset]. U.S. Geological Survey, Astrogeology Science Center. Retrieved from https://astrogeology.usgs.gov/search/map/moon_lro_lroc_wac_global_morphology_mosaic_100m

USGS. (2015). *Lunar Orbiter Laser Altimeter and Kaguya Terrain Camera Digital Elevation Model* [Dataset]. U.S. Geological Survey, Astrogeology Science Center. Retrieved from https://astrogeology.usgs.gov/search/map/moon_lro_lola_selene_kaguya_tc_dem_merge_60n60s_59m

Whitford-Stark, J. L. (1982). Geologic studies of the lunar far side crater Tsiolkovsky. In *13th lunar and planetary science conference* (pp. 861–862).

Wieczorek, M. A., Jolliff, B. L., Khan, A., Pritchard, M. E., Weiss, B. P., Williams, J. G., & Bussey, B. (2006). The constitution and structure of the lunar interior. *Reviews in Mineralogy and Geochemistry*, *60*(1), 221–364. https://doi.org/10.2138/rmg.2006.60.3

Wieczorek, M. A., Neumann, G. A., Nimmo, F., Kiefer, W. S., Taylor, G. J., Melosh, H. J., et al. (2013). The crust of the Moon as seen by GRAIL. *Science*, *339*(6120), 671–676. https://doi.org/10.1126/science.1231530

Wright, J., Zambon, F., Carli, C., Altieri, F., Pöhler, C. M., Rothery, D. A., et al. (2024). A geostratigraphic map of the Rachmaninoff basin area: Integrating morphostratigraphic and spectral units on Mercury. *Earth and Space Science*, *11*(2), e2023EA003258. https://doi.org/10.1029/2023EA003258

Yamamoto, S., Nakamura, R., Matsunaga, T., Ogawa, Y., Ishihara, Y., Morota, T., et al. (2010). Possible mantle origin of olivine around lunar impact basins detected by SELENE. *Nature Geoscience*, *3*(8), 533–536. https://doi.org/10.1038/ngeo897

Zambon, F., Carli, C., Altieri, F., Combe, J.-P., Van Der Bogert, C. H., Poehler, C. M., et al. (2021). Spectral analysis of Apollo Basins on the Moon through spectral units identification. *EGU General Assembly*, *2020*, EGU21–15831. https://doi.org/10.5194/egusphere-egu21-15831

Zambon, F., Carli, C., Wright, J., Rothery, D. A., Altieri, F., Massironi, M., et al. (2022). Spectral units analysis of quadrangle H05-Hokusai on Mercury. *Journal of Geophysical Research: Planets*, *127*(3), e2021JE006918. https://doi.org/10.1029/2021JE006918

Zhang, X., & Cloutis, E. (2021a). Near-infrared spectra of lunar ferrous mineral mixtures. *Earth and Space Science*, *8*(4), 1–15. https://doi.org/10.1029/2020EA001153

Zhang, X., & Cloutis, E. (2021b). Variations in the near-infrared spectral properties of ferrous mineral mixtures with different relative abundances. *Earth and Space Science*, *8*(9), 1–11. https://doi.org/10.1029/2021EA001636